Power and dynamic performance of a floating multi-functional platform: an experimental study

Yu Zhou[1, 2, 3], Lifen Chen[1, 3], Jie Zhao[4], Xiangjian Liu[4], Xiaorong Ye[4], Fei Wang[4], Thomas A.A. Adcock[2], Dezhi Ning[1, 3*]

State Key Laboratory of Coastal and Offshore Engineering, Dalian University of Technology, Dalian, China

Department of Engineering Science, University of Oxford, Oxford, UK

Dalian Key Laboratory of Offshore Renewable Energy, Dalian University of Technology, Dalian, China

Dalian Shipbuilding Industry Design & Research Institute Co. LTD., Dalian, China

Abstract

Hybrid platforms which integrate a floating offshore wind turbine and a wave energy converter are a promising technology as the wave energy converter can lead to a more stable platform and potentially lower costs. In the present work, a semi-submersible floating offshore wind turbine platform integrating with an array of wave energy converters (WECs) in the form of an oscillating water column (OWC) is presented and tested experimentally. The hydrodynamic properties of the multi-functional platform were investigated under a series of regular and irregular wave tests considering both operational and survival sea states. The influence of various parameters (including incident wave directions and chamber opening ratios) on the dynamic responses and the wave energy capturing were systematically studied. The introduction of the oscillating water column can not only capture wave energy but also reduce the heave, roll and pitch responses, especially for long waves $kh \leq 2.0$, $kh \leq 1.4$ and $kh \leq 1.76$ respectively. The maximum reduction in heave, roll and pitch are 35%, 55.4% and 13.8%, respectively. The chamber air orifice size was analyzed and optimized. From the survival sea state tests, it is found that the introduction of the OWC WECs decreases the maximum amplitudes of the platform motions in all five freedoms and the nacelle acceleration.

Keywords: Multi-functional platform; OWC-WEC; Motion reduction; Wave energy;

* Corresponding author.
Email address: dzning@dlut.edu.cn (D.z. Ning).

Experiment.

1. Introduction

Recently, wind turbine technology is developing quickly with engineering improvements and the industry is growing towards maturity. The Levelized Cost of Energy (LCOE) of bottom-fixed offshore wind turbines declined by 60% between 2010 and 2021, from USD 0.188/kWh to 0.075/kWh [1]. However, the available sites suitable for applying fixed wind turbines are relatively limited. Thus, researchers are starting to develop floating solutions for offshore deep waters. Floating Offshore Wind Turbine (FOWT) is still in an early stage of development with a high LCOE. The primary concerns are its capability for providing stable working conditions for wind turbines, and the ability of their operators to assess the platform offshore [2]. One attractive solution is the combined exploration of wind and other ocean energies, leveling the total investment and enhancing the performance in terms of stability and total energy capturing.

Ocean wave energy is another promising renewable energy that is abundant but is currently too expensive for exploitation on its own [3]. Many sites suitable for exploring wind energy using FOWT also have significant wave resources—this is a challenge for platform stability but an opportunity in terms of wave energy capture. Multi-functional integration between FOWT and wave energy converter (WEC) makes efficient use of ocean space and reduces construction costs [4]; the two technologies can share a common floater (i.e. the multi-functional platform), mooring system and power transfer facility. In addition, ocean waves are more consistent when compared to offshore wind, which reduces the periods of zero electricity production of the whole system [5]. To date, the multi-functional platform is still in the conceptual design stage.

The combined exploitation of offshore wind and wave energy has attracted increasing interest in the last few years. The assessment of the offshore wind and wave energy resources [6, 7]; the issue analysis of the electricity production from the combined system [8, 9], and the hydrodynamic and optimization analyses of the multi-functional platform [10, 11] are investigated. It is well acknowledged that the addition of a wave energy device to an offshore

wind platform has the benefit of providing an additional power source for the system [12].

Currently, two types of WECs are extensively used for the multi-functional integration: Oscillating Body (OB)- [13] and Oscillating Water Column (OWC) -type [14] WECs. The OB-type WEC converts the wave energy into electricity through the buoys' heaving, rolling, or pitching motions [15]. Thus, the motion modulation between the OB-type WEC and the wind turbine foundation is a challenging task; the WEC is in favor of larger structure motion for extracting more wave energy while the opposite is true for floating offshore wind turbine foundations for providing more stable work conditions. The multi-functional platform usually has a larger water-plane area, which may increase the 2^{nd}-order platform motions [16]. The Power Taken Off (PTO) system of the OB-type WECs is generally optimized for the largest wave power generation with the increased motion response [17]. Gao et al. [18] predicted the platform motion, the PTO force and the power production of an OB-type WEC combined with a spar-type wind turbine platform. The result shows that the strong resonant heave motion of the OB-type WEC leads to a significant variation in the buoyancy force, and large wave-slamming forces are observed.

Unlike the OB-type WEC, the OWC-type WEC converts wave energy through the oscillation of water columns inside chambers [19]. It has a no-moving chamber underwater, which could improve the stability and reliability of such the multi-functional integration platform [20]. Improved stability allows the wind turbine to operate in more severe sea conditions and reduces the loads on the system. Therefore, the integration of an OWC-type WEC is examined in the present study.

A series of theoretical and experimental studies have been carried out to exploit the dynamic response and the power output of a FOWT-OWC platform of various designs. Based on the linear wave theory, a significant quantity of simplified models have been established to perform the dynamic analysis of a FOWT-OWC platform [21-24]. These simplified models are efficient and fast tools for preliminary design and optimization [25, 26]. However, the nonlinear and viscous properties of the fluid are generally overlooked, which may lead to under- or over-design of such the multi-function platform [27].

Physical model tests have also been widely used, which model more complex behaviors of an offshore platform comprehensively and realistically [14]. It is a mature procedure for carrying out a series of static and dynamic model testing. The coupled hydrodynamics of the FOWT-OWC platform has been the focus of much previous work using an experimental approach. Zhu et al. [28] performed an experimental study on the hydrodynamics of a semi-submersible platform consisting of a FOWT and an OWC-type WEC. The results show that the pitch motion of the platform can be reduced by 60% with a proper control over the valve for opening/closing the OWC orifice, although the energy capturing efficiency of the WEC is decreased by about 50%. Zhang et al. [29] also experimentally assess the effect of the PTO control on the dynamic performance of a semi-submersible FOWT-OWC platform. An informed selection of PTO control strategy was shown to be able to reduce the platform pitch motion and fatigue loads on the tower base. In contrast, Sarmiento et al. [30] carried out an experimental campaign to investigate the dynamic response of a semi-submersible FOWT-OWC platform under both operational and survival sea states (coupled wave-wind-current conditions are considered). It is found that either a fully or a partially open OWC chamber has limited influence on the surge, heave and pitch motions of the platform. Fenu et al. [31] experimentally analyzed the dynamic behavior and the power performance of a spar-type FOWT integrated with three OWC WECs. It is found that the use of the OWC device increases the overall power productivity without significantly affecting the platform motion. Further, Aubault et al. [32] argued that the pitch and roll motions of the platform would increase if the two OWCs integrated into a semi-submersible WindFloat platform shared one PTO system based on their frequency domain analysis and physical experiments. Zhou et al. [20] carried out a spar-type FOWT-OWC experiment and debated that the introduction of the OWC device can reduce the heave motion of the platform by up to 54.1%. Obviously, the hydrodynamics of the FOWT-OWC integrating system are complex, and more hydrodynamic analyses are required. In addition, the above experimental studies tested the semi-submersible platform motions only in the surge, heave and pitch. More analysis and discussion of the freedoms in sway and roll should be carried out.

In the present work, a semi-submersible FOWT platform with/without OWCs was tested using carefully instrumented physical model testing. The primary objective is to investigate the effect of the introduction of an OWC on the hydrodynamic properties of the FOWT platform. The rest of the paper is organized as follows. Section 2 describes the experimental setup and data analysis. Section 3 presents the experiment repeatability. In Section 4, the hydrodynamics of the FOWT-OWC platform under regular and irregular waves are presented and discussed. Finally, conclusions are summarized in Section 5.

2. Experiment

2.1 Experimental setup

The FOWT-OWC was designed to be a triangular semi-submersible platform for a 10 MW wind turbine. It consists of three columns (labeled as C1, C2 and C3) bounded by a series of submerged beams and upper braces. Both the columns and the submerged beams were designed to provide buoyancy for the platform. Three OWC devices (namely OWC1, OWC2 and OWC3) were installed concentrically inside the columns. The main dimensions of the model FOWT-OWC at a scale of 1:50 are shown in Fig. 1, and Fig. 2 is a photo showing the model fabricated in the laboratory. A wind turbine tower was installed at the column C2. The whole platform is treated as a rigid body, and the flexibility of the wind turbine tower is not considered.

The physical model tests were performed in a wave flume at the State Key Laboratory of Coastal and Offshore Engineering, Dalian University of Technology, China. The flume is 60 m in length, 4 m in width, and 2.5 m in deep. Fig. 3 shows a sketch of the wave flume and the experimental setup. The model FOWT-OWC was placed in the middle of the flume at a location approximately 18 m away from the wave maker. h denotes the water depth. For convenience, we introduce a Cartesian coordinate system with its origin at the still water level and the geometric center of the FOWT-OWC model in the plane view, as shown in Fig. 3. In addition, the FOWT platform without OWC was also investigated experimentally for comparison in the present experiments.

In this work, a horizontal soft mooring system was used to restrain the horizontal motions (i.e., surge, sway and yaw) while allowing unrestricted vertical motions (i.e., heave, pitch and

roll). Both the FOWT and FOWT-OWC platforms share the same mooring system. The mooring system consisted of 4 horizontal spring wires orientated from the model to the tank sides. The total stiffness of the system in the horizontal direction was approximately 0.02 kN/m. In this case, the natural period of the system in the horizontal direction was $T_{\text{nature}} \geq 5.66$ s ($T_{prototype} \geq 40$ s at full scale), away from the predominant ocean wave frequencies of concern.

The ratio of the column radius and its minimum distance to the flume wall was 0.112, which is smaller than 0.2 [33]. In addition, the water-plane area of the submersible platform is small (one of the advantages of its application) and hence the reflection from the tank side walls was considered to be small.

Tables 1 and 2 summarize the main characteristics of the FOWT and FOWT-OWC models, where I and R are the inertial and the radius of gyration of the platform, respectively. Both the FOWT and FOWT-OWC are designed for similar inertial parameters. Table 3 lists the variation in terms of the mass and the radius of gyration, which was less than 10% after the integration of the OWC devices.

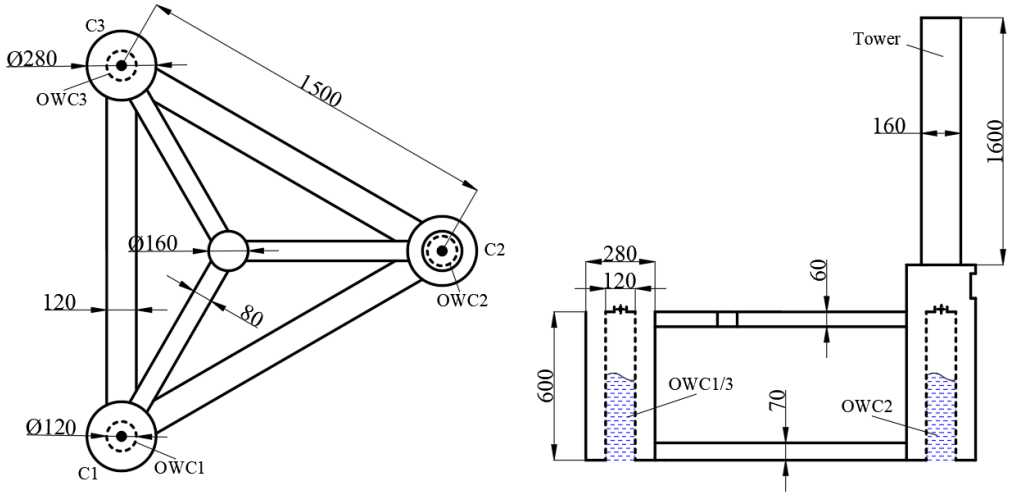
Fig. 5 gives the GZ curve of the FOWT-OWC platform, which denotes the transverse distance between the center of gravity (G) and buoyancy with a certain heeling angle. Another measure of the stability of the platform is the metacentric height, which was 0.814 m measured from the platform bottom.

The dynamic responses of the platform are also associated with the pneumatic air induced by both PTO and water columns inside chambers (namely the chamber water columns hereafter). The effect of the PTO damping was conceptualized by the circular air orifice, as suggested by [14]. Table 4 summarizes the opening ratios and the corresponding areas of the circular orifices considered. The opening ratio is expressed as $\varepsilon = S_{\text{orifice}} / S_{\text{OWC}}$, where S_{orifice} and S_{OWC} are the cross-sectional areas of the circular orifice and the circular chamber, respectively [34]. Note that the maximum opening ratio, $\varepsilon = 15\%$, was the case of the completely opened OWC chamber.

A series of regular and unidirectional irregular waves were generated in the wave flume to interact with the experimental models. Table 7 presents the regular waves in the range of 1.13

$\leq kh \leq 2.81$ with the corresponding wave steepness of $0.074 \leq kA \leq 0.095$, where k is the wave number, A is the wave amplitude, and T is the wave period. The wave amplitude generally increases with the wave length. Table 8 gives the details of the irregular waves considered, where T_p is the peak wave period and H_s is the significant wave height. Both operational and survival sea states were considered, and the latter corresponds to the extreme wave at a 100-year return period in a random sea. The JONSWAP spectrum with the peak enhancement factor of $\gamma = 3.3$ was utilized. In addition, three different wave incidences ($\beta = 0$, $\pi/2$, and π as shown in Fig. 4) were considered, which were realized by rotating both the experiment model and the mooring lines clockwise around the center of gravity (COG) with corresponding angles.

In order to monitor the free surface elevation inside the OWC chambers, three YWH200 - D type wave gauges (i.e., G1 – G3) were installed at each OWC chamber center. Table 5 presents the positions of the wave gauges; wave gauge G4 was located at the position (0.1 m, 0 m, 0 m) to measure the free surface elevation around the COG of the platform. One CY200-type pressure sensor was used to measure the air pressure inside the chamber. The pressure sensor can measure up to 10 kPa, and the measurement error is 0.1%FS (Full scale), and was calibrated by carrying out hydrostatic pressure testing. All pressure sensor readings recorded a measurement of 1.96 kPa at a still water depth of 0.2m. An additional seal is employed to ensure the air-tightness. An optical motion capturing system (Optotrak Certus) was applied to measure the platform motions (surge, sway, heave, roll and pitch). The accuracy and resolution are 0.1 mm and 0.01 mm, respectively. The platform movements in surge, heave and pitch were measured under the wave direction $\beta = 0$, and the roll and sway motions were under $\beta = \pi/2$. In order to analyze the inertial forces induced by the platform movements, two YGS20X-XX-type wireless accelerometers were installed at the nacelle and the deck, respectively. It can simultaneously measure acceleration in the X-, Y-, and Z-directions. Table 6 gives the positions of the accelerometers. The sampling rate for all these measurements was 100 Hz. Fig. 6 shows the measuring instruments in the experiments.



(a) Top view (b) Side view

(c) Front view

Fig. 1. Main dimensions of the FOWT-OWC (Units mm).



Fig. 2. Photo of the FOWT-OWC platform.

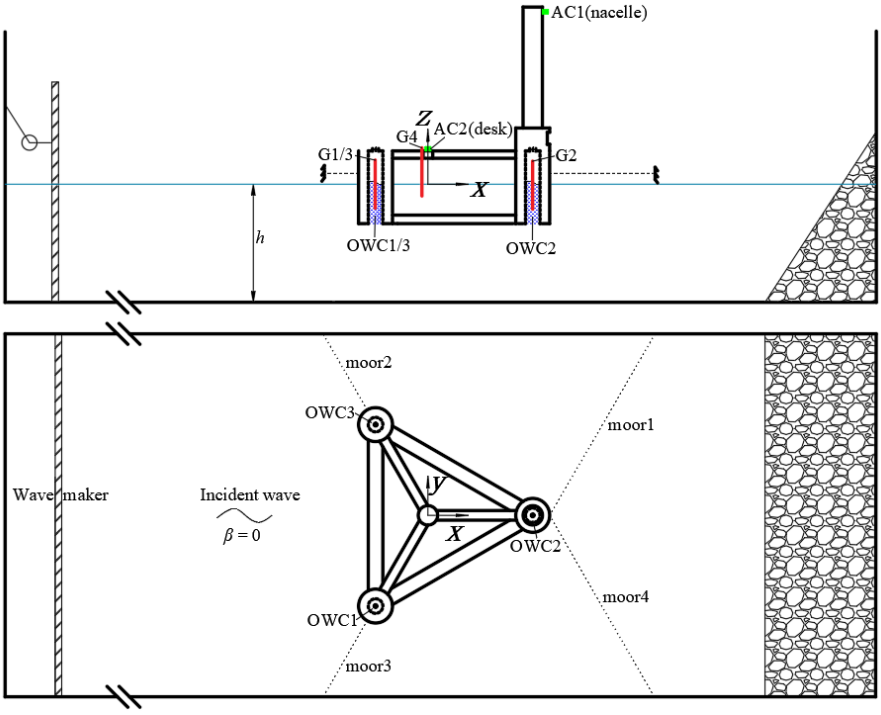
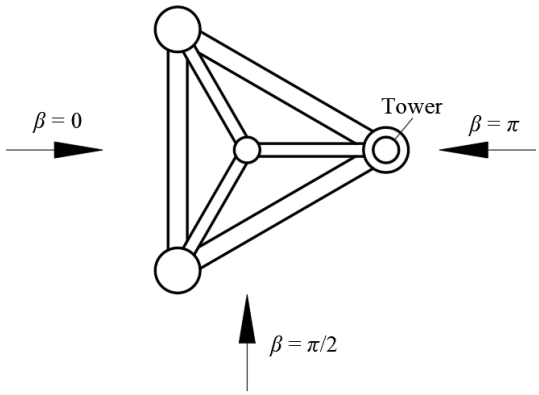


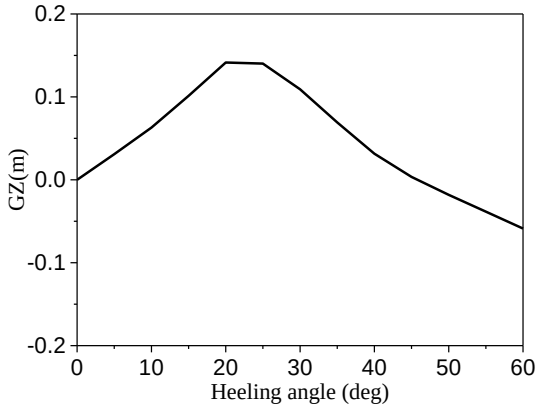
Fig. 3. Sketch of the experimental setup.



206

207 Fig. 4. Definition of the incident wave direction.

208



209

210 Fig. 5. GZ curve of the FOWT-OWC platform.

211





212

213 (a) Wave gauge (b) Pressure sensor





(c) Motion capture system (d) Accelerometer

Fig. 6. Experimental measuring instruments.

Table 1. Main characteristics of the FOWT model.

Platform mass (kg)	96	I_{xx} (kg m^2)	77.4	R_x (m)	0.898
Platform draft (m)	0.35	I_{yy} (kg m^2)	83	R_y (m)	0.930
Center of gravity (m)	(0, 0, 0.08)				

Table 2. Main characteristics of the FOWT-OWC model.

Platform mass (kg)	90.2	I_{xx} (kg m^2)	64	R_x (m)	0.842
Platform draft (m)	0.39	I_{yy} (kg m^2)	66	R_y (m)	0.860
Center of gravity (m)	(0, 0, 0.077)				

Table 3. Ratios of variation in the inertial parameters.

Platform mass	6.0%
Radius of gyration R_x	6.2%
Radius of gyration R_y	7.5%

Table 4. Opening ratios and areas of the chamber orifices.

Opening ratios ε	0%	1%	3%	15%
$S_{orifice}$(cm^2)	0	1.1	3.4	17

Table 5. Positions of the wave gauges.

	Position(m)		Position(m)
G1	(-0.43, 0.75, 0)	G2	(0.87, 0.75, 0)
G3	(-0.43, -0.75, 0)	G4	(-0.1, 0, 0)

Table 6. Positions of the accelerometers.

	Position(m)		Position(m)
AC1	(0.94, 0, 1.77)	AC2	(0, 0, 0.21)

Table 7. Regular wave conditions.

T (s)	2.10	1.95	1.85	1.80	1.60	1.56	1.44	1.35	1.25	0.99
kh	1.13	1.26	1.34	1.40	1.69	1.76	2.00	2.42	2.60	4.1
A (cm)	6.87	5.85	5.55	5.60	4.35	4.30	3.83	3.45	3.30	3.37

Table 8. Irregular wave conditions.

	Operational sea states	Survival sea states	
T_p(s)	1.06	2.22	2.54
H_s(cm)	30	17.8	21

2.2 Data analysis

The pneumatic power inside the OWC chamber is associated with the periodic oscillation of the chamber water column. The incident wave energy is converted into the pneumatic air by the chamber oscillating water column. The pneumatic air can be used to pump the turbine connected to the generator to generate electricity. Air compressibility was ignored in the present scaled model tests [35]. Thus, the captured pneumatic power can be calculated from the measured chamber air pressure p and the air volume flux Q through the air orifice [36]:

$$P_{\mathrm{owc}} = \frac{1}{T}\int_t^{t+T} p(t)\cdot Q(t)\,dt = \frac{S_{\mathrm{OWC}}}{T}\int_t^{t+T} p(t)\cdot \eta_{\mathrm{OWC}}(t)\,dt \tag{1}$$

where η_{OWC} denotes the averaged chamber surface elevation. It is measured by wave gauges (G_1-G_3) inside the OWC chamber. This is reasonable as the wavelength is much longer than the chamber diameter. The spatial variation of the free surface inside the chamber can be ignored.

For the regular wave, the averaged energy flux per unit width of the incident wave (i.e., P_{inc}^{r}) is

$$P_{\mathrm{inc}}^{\mathrm{r}} = \frac{\rho g A^2 \omega}{4k}\left(1+\frac{2kh}{\sinh 2kh}\right) \tag{2}$$

where ρ is the water density, g is the acceleration due to gravity, and ω is the frequency determined by the linear dispersion relationship $\omega^2 = gk\tanh(kh)$.

For the calculation of incident wave energy under irregular waves, the results of different methods vary greatly. In the present experiment, the empirical formulas from ITTC (International Towing Tank Conference) were used, and there are [37]:

$$P_{\mathrm{inc}}^{\mathrm{irr}} = \frac{\rho g^2 H_s^2 T_E}{64\pi} \tag{3}$$

where T_E is the energy period and is defined by:

$$T_E = \alpha T_p \tag{4}$$

where α is the shape parameter. When the irregular spectrum is P-M spectrum, $\alpha = 0.86$, and JONSWAP spectra, $\alpha = 0.9$.

Thus, the relative capturing width is calculated:

$$\mu = \frac{P_{\text{owc}}}{D_{\text{owc}} P_{inc}}. \tag{5}$$

where $D_{\text{owc}} = 0.12$ m is the diameter of the chamber water column.

3. Experimental repeatability

In the present experiment, each test case was replicated at least twice in order to establish the repeatability and accuracy of the experimental results. The measured time histories of the FOWT and FOWT-OWC platforms are compared in Appendix A. The measured platform motions, accelerations, chamber air pressure and surface elevation for the duplicated tests show good agreement, indicating that the experiments exhibit strong repeatability and are robust.

4. Results and Discussions

4.1 Free decay tests

Free decay tests were first carried out to identify the characteristics of the platform with and without OWC devices. The platform was free-floating, and only free decay tests for heave, pitch and roll motions were performed. The maximum opening ratio $\varepsilon = 15\%$ was selected for the FOWT-OWC model, and it can be used for the case of the totally opened OWC chamber.

The time series and the corresponding amplitude spectra of the measured motions in the free decay tests aforementioned are plotted in Figs. 7 (model FOWT) and 8 (model FOWT-OWC). It can be seen that, with the installation of the OWC device, the natural periods in heave, roll and pitch are increased by 8.63%, 7.8% and 7.52%, respectively. The natural period can be expressed as

$$T_{\text{n}} = 2\pi[(m+m_{\text{a}})/C]^{0.5} \tag{6}$$

Here, $C = \rho g A_{\text{WP}}$ is the water resilience stiffness with A_{WP} being the water-plane area, m and m_{a} are the mass and the added mass of the system, respectively [38]. We know from Tables 1 and

2 that both the mass and the inertia of the platform decrease when the OWCs are integrated. The corresponding water resilience stiffness also reduces due to the smaller water plane area. Thus, the water resilience C is identified as a dominant factor for the observed increase in the natural periods considering these two have opposite effects.

In addition, it can be seen from Figs. 7(a) and 8(a) that the heave motion curves also show peaks at lower frequencies (i.e. ω = 1.91 or 1.8 rad/s), which are very close to the nature periods in pitch or roll. This may result from the strong coupling between the heave and pitch/roll motions associated with the uneven mass distribution of the (model FOWT and FOWT-OWC) platforms. Small disturbances in pitch or roll may thus be amplified and transferred into heave motions [39]. Recall that the platform was lifted to a certain height above the mean water level manually (i.e. initial vertical displacement) and then was released to heave freely during the heave-free-decay-test. The platform may incline slightly towards the bow/stern or starboard/portside during this manually lifting process, resulting in a small initial disturbance in roll and pitch. The small inaccuracy in determining/locating the platform COG in the experiments would be another possible reason. The marker of the NDI motion capturing system was supposed to be installed at the COG, otherwise the distances between the marker and the COG should be provided to transfer the motion measurements back to the COG. The roll- or pitch-induced vertical motions may be misinterpreted as heave motions if these errors in COG locations were introduced.

The effect of the opening ratio on the natural periods of the platform was also investigated, as shown in Table 9. It can be seen that the effect of the opening ratio on the natural periods is negligible when its value exceeds 1%. While the heave, roll and pitch natural periods are decreased by 5.14%, 7.23% and 11.66%, respectively, when ε decreases to 0%. This is also due to the increased wave resilience (shown in Eq. (6)), which makes a major contribution to the decrease of the natural periods. Thus, a further refinement of the opening ratios ($\varepsilon \leq 1\%$) should be considered in the future.

In addition, the dynamic characteristics of the rotated platform are investigated, as shown in Table 10. Recall that the platform was rotated in this work for modeling various wave incident

angles. The results for cases with and without the mooring system are also included. It is clear from Table 10 and Table 9 that the heave, roll and pitch nature periods change less than 5% with the attachment of the present horizontal mooring system. And the pitch nature period for the model layout of $\beta = 0$ and $\pi/2$ are also similar. This confirms that both the mooring system and the model layout have less influence on the inherent characteristics of the platform.

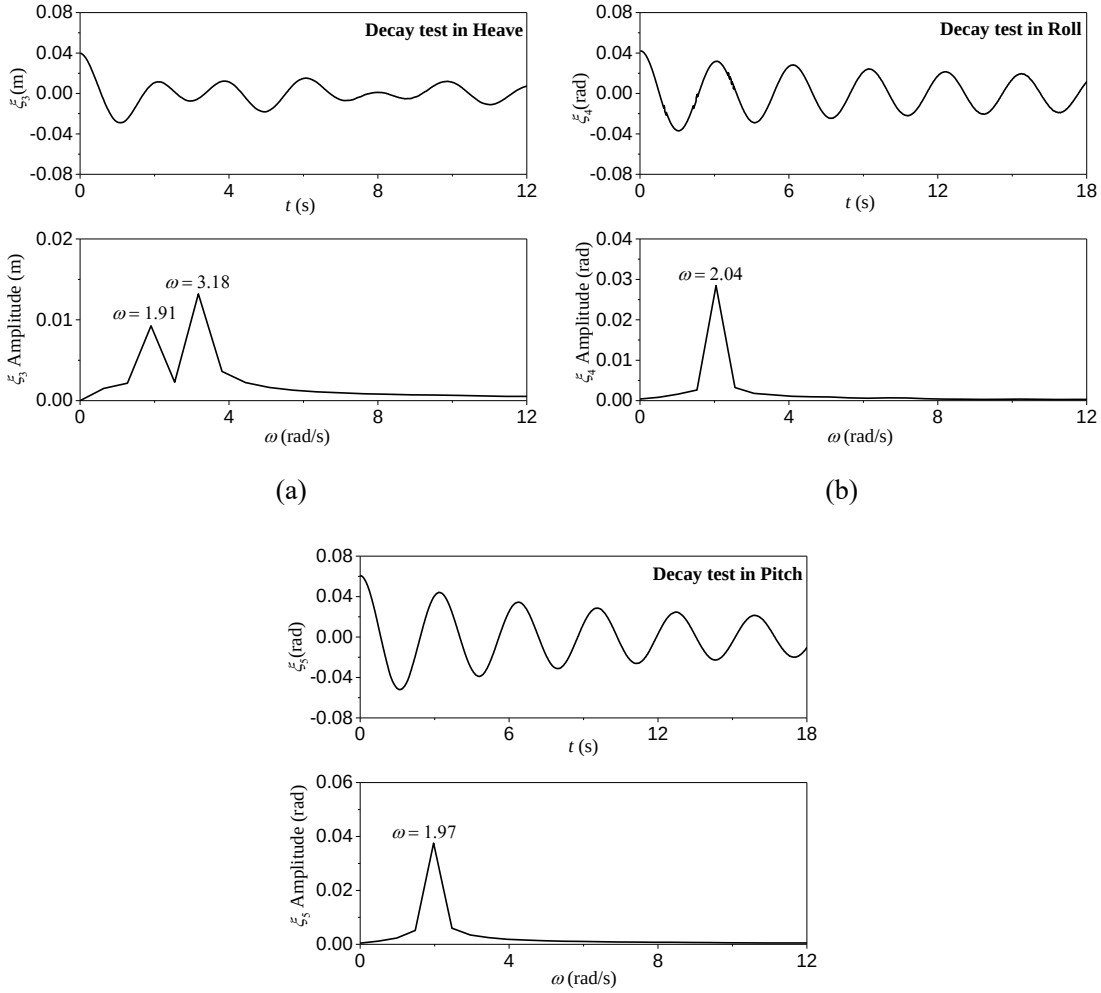
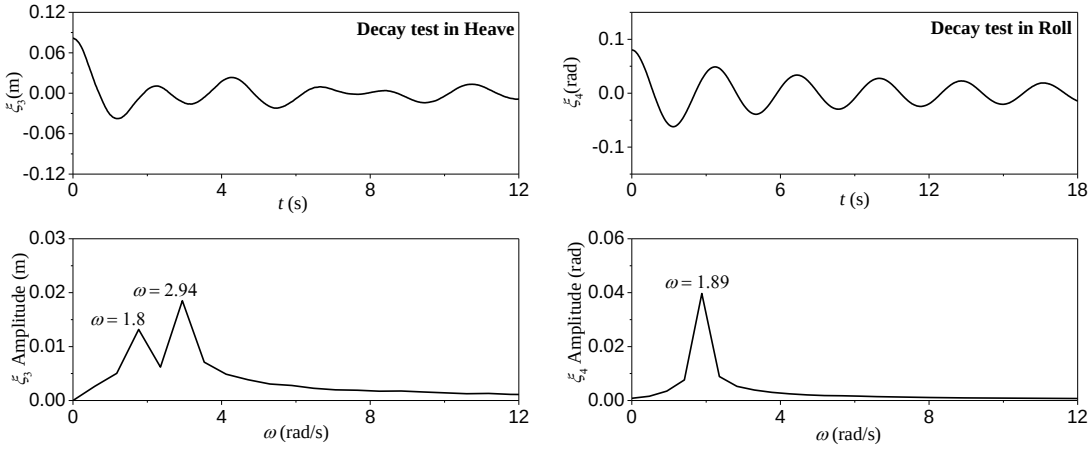
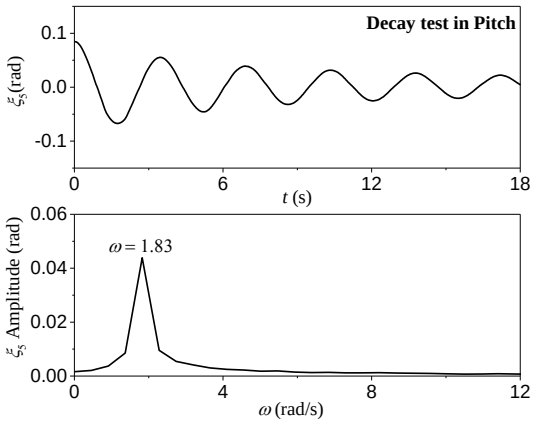


Fig. 7 Decay tests of the FOWT platform: Time series and the amplitude spectra in (a) heave (b) roll and (c) pitch ($\varepsilon = 15\%$).



(a) (b)



(c)

Fig. 8 Decay tests of the FOWT-OWC platform: Time series and amplitude spectrum results in (a) heave (b) roll and (c) pitch (ε = 15%).

Table 9. Natural periods of the platform.

	FOWT	FOWT-OWC (0%)	FOWT-OWC (1%)	FOWT-OWC (3%)	FOWT-OWC (15%)
T_{heave} (s)	1.97	2.03	2.12	2.15	2.14
T_{roll} (s)	3.08	2.95	3.32	3.33	3.32
T_{pitch} (s)	3.19	3.03	3.42	3.42	3.43

Table 10. Natural periods of the horizontally-moored platform rotated at various angles.

	FOWT ($\beta = 0$)	FOWT ($\beta = \pi/2$)	FOWT-OWC ($\beta = 0$)	FOWT-OWC ($\beta = \pi/2$)
T_{heave} (s)	1.98	-	2.12	-
T_{roll} (s)	2.95	-	3.17	-
T_{pitch} (s)	3.06	3.06	3.26	3.25

4.2 Regular wave tests

In this section, the hydrodynamic properties of the horizontal-moored FOWT-OWC are discussed under a series of regular waves (shown in Table 7). Three different air orifice opening configurations were examined: the completely closed (ε = 0%), the partially opened (ε = 3 %) and the completely opened (ε = 15 %). The effects of the incident directions (β = 0, π/2 and π) were also considered. It should be noted that all the measurements were analyzed at a steady state.

4.2.1 Hydrodynamic responses

Fig. 9 presents the Response Amplitude Operators (RAOs, $\triangle\xi/A = (\xi_{crest}-\xi_{trough})/2A$) of the model FOWT-OWC during the regular wave tests. The corresponding results for the FOWT platform are also illustrated for direct comparisons. Noted that the surge, heave and pitch were measured under the wave direction $\beta = 0$, and for the roll and sway $\beta = \pi/2$. In addition, the yaw motion was not shown for its smaller amplitude compared to other degrees of freedom.

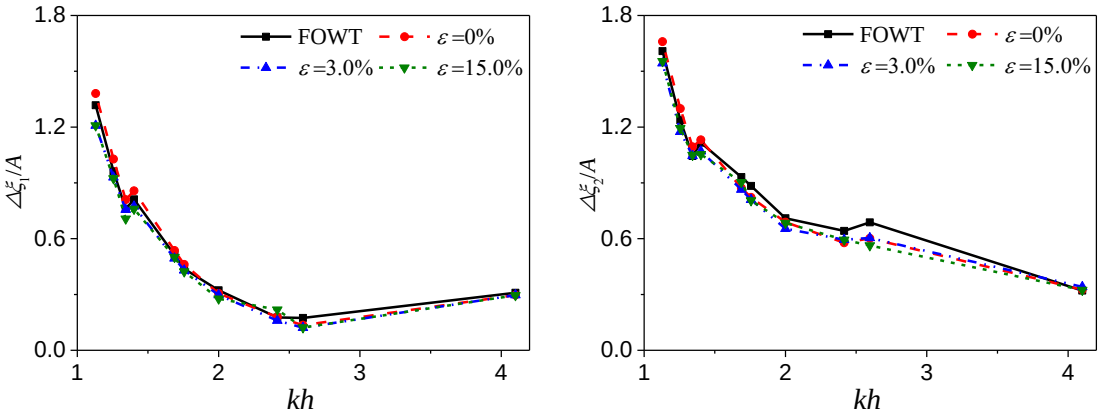
It can be seen from Figs 9 (a-b) that both the surge and sway RAOs for the proposed FOWT and FOWT-OWC are similar. This is expected, as these two motions are associated with the outside wetted surface area of the platform, which is not changing even when the OWCs are introduced.

In contrast, the variations in heave, roll and pitch RAOs (see Fig. 9 c–d) are relatively large, resulting from the oscillation of the water columns inside the chambers. Additional added mass and damping are introduced. More specially, the heave RAOs are reduced across the whole range of wave conditions considered but more at lower frequencies, while the consistent reduction in the roll RAOs is only found at higher wave frequencies ($kh \leq 1.75$). The pitch RAOs for the FOWT are always in between when compared to the FOWT-OWC of various opening ratios. It should be noted that the draft of the FOWT-OWC is a little larger than that of the FOWT, which can lead to a slight reduction in the heave RAOs. Yet, its influence is relatively limited.

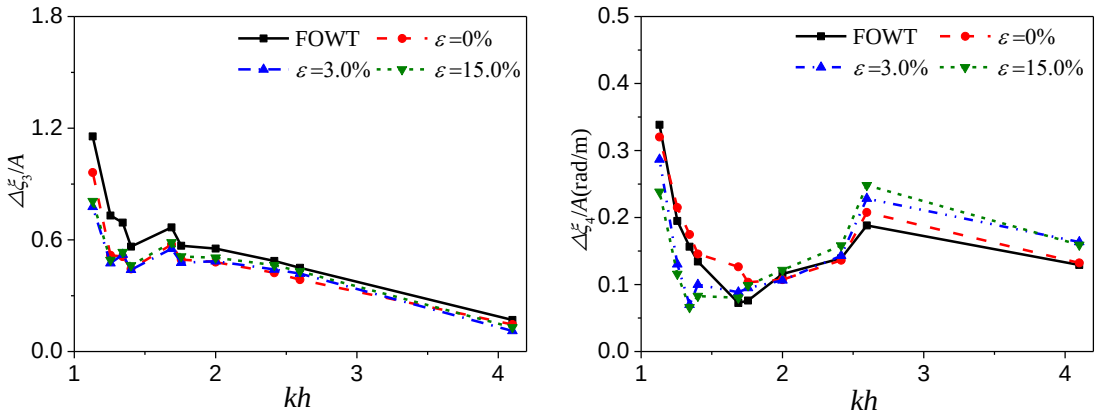
From the Figs. 9(d) and (e), it further can be seen that the rotational RAOs become smaller when the air orifice is completely closed (ε = 0%). The enclosed chamber can greatly suppress

the oscillation of the chamber water column, and hence provide an optional solution for a stable operation at $kh = 2.6$. Yet, this should be avoided in the low frequency domain ($kh \leq 1.8$), where the rotational RAOs increase. Thus, it can be concluded that the introduction of the OWCs can not only capture wave energy but also reduce the heave, roll and pitch RAOs, especially for long waves with larger periods.

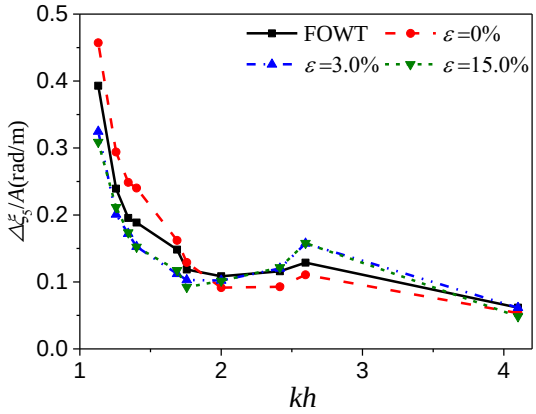
In addition, it can be seen that there exists a peak RAO in roll and pitch for both FOWT and FOWT-OWC models at about $kh = 2.6$. The relative space between the incident wave and the model characteristic lengths is close to 1.5 here, and thus the wave peaks and troughs act on the two legs of the platform at the same time, leading to a larger rotational amplitude. This can be confirmed by the time series of the free surface elevation inside the chambers of the OWC1 and OWC2 in Fig. 10. Two incident wave directions $\beta = 0$ and $\pi/2$ are plotted. Due to the interaction of the wave crests and troughs, the chamber water columns oscillate in an opposite phase. And it leads to a larger rotational motion as mentioned above.



(a) (b)

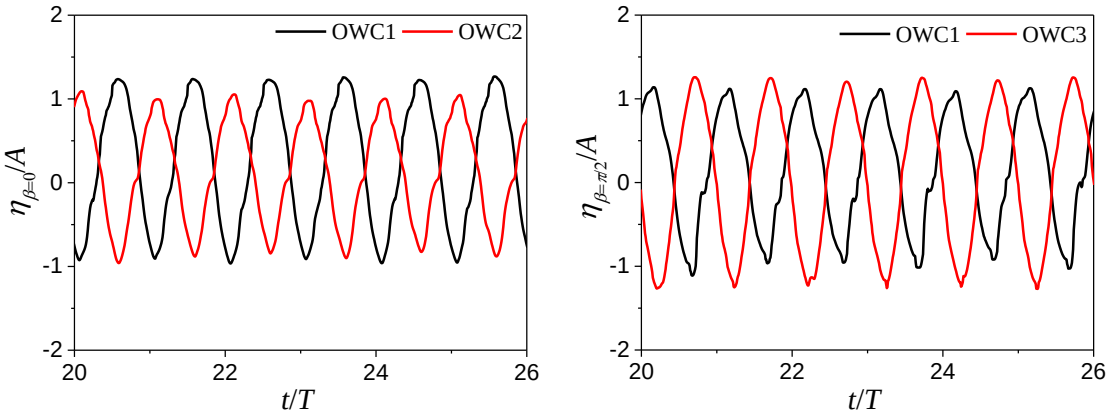


(c) (d)



(e)

Fig. 9 The RAOs of the FOWT and FOWT-OWC platforms in (a) surge, (b) sway, (c) heave, (d) roll and (e) pitch motions with *kh*.



(a) (b)

Fig. 10 Time series of the surface elevations inside the chambers for (a) $\beta = 0$ and (b) $\beta = \pi/2$ at $kh = 2.6$ (ε = 3 %).

4.2.2 Wave energy capturing

In this subsection, the effect of the chamber opening ratio on its wave energy capturing capability is investigated. The hydrodynamics of the OWC1 are discussed firstly with the incident wave direction β = 0. Figs.11 (a-c) illustrates the variations of the three main parameters of concern against kh. These are the chamber air pressure characterized by $\triangle P_{\text{air}} = (P_{\text{crest}}\text{-}P_{\text{trough}})/2$, the free surface elevation characterized by $\triangle \eta = (\eta_{\text{crest}}\text{-}\eta_{\text{trough}})/2$, and the relative capturing width μ, respectively. The pneumatic power of the OWC1 at full scale is also plotted in Fig. 11(d). The scale factor for the prototype pneumatic power is $50^{3.5}$.

As shown in Figs. 11(a)-(b), the chamber air pressure and the free surface elevation show an opposite variation trend when the opening ratio increases from 1% to 15%. This is associated with the decrease of the PTO damping with the opening ratio. The free surface elevation inside chambers is observed to be the largest for ε = 15% at kh = 2.42 (i.e., the heave natural period of the OWC chamber). And the corresponding air pressure inside chambers here is small as the chamber is nearly fully opened when ε = 15%. Regarding the minimum opening ratio ε = 1 %, the maximum pressure occurs in the lower frequency domain due to the fact that a larger PTO damping shifts the resonance frequency of the OWC to the lower range [40].

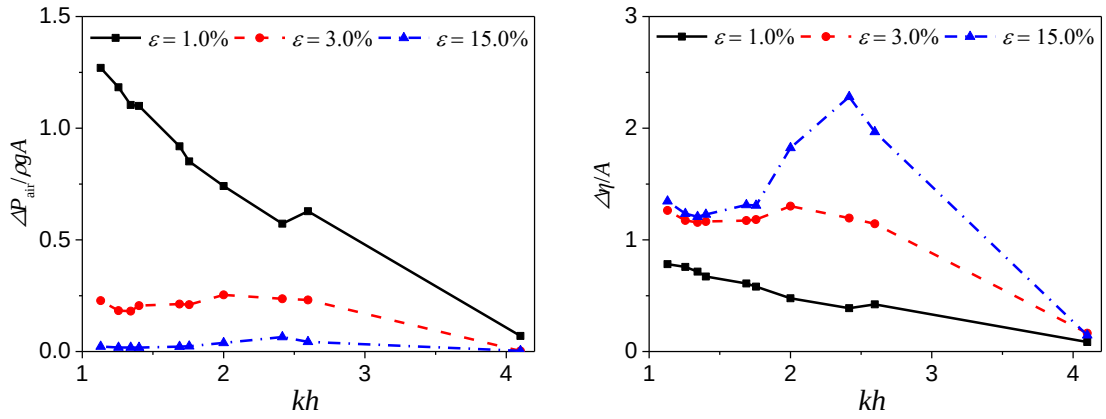
It can be seen from Figs. 11(c)-(d) that the opening ratio also has a great influence on the relative capturing width and the pneumatic power, and the trend is complex. In the intermediate and high frequency domain ($kh \geq 1.76$), the optimal opening ratio is found to be ε = 3% with which the largest relative capturing width is generated. The maximum relative capturing width is μ = 0.12 at kh = 2.6. A similar observation was captured for a sole cylindrical OWC device of a larger geometry [14]. While in the low frequency domain $kh \leq 1.76$, the optimal opening ratio is shifted to a smaller value. The opening ratio ε = 1% produces the largest relative capturing width, the optimal opening ratio should be a smaller value, i.e., $\varepsilon_{\text{optimal}} \leq 1\%$. Further study is needed to determine the optimal opening ratio in the low frequency domain.

In Fig. 11(d), the pneumatic power at full scale is found to decrease with kh. This is due to the increase of the incident wave energy, which has a quadratic increase with the incident wave amplitudes, as shown in Eq. (2). The pneumatic power increases for waves of lower frequency

412 even though the relative capturing width decreases (the level of the increase in the incident
413 wave energy is larger than that of the captured wave energy). Therefore, the optimal opening
414 ratio needed to be selected by considering the offshore marine environments.

415 The characteristics of the relative capturing widths of the three OWCs are further studied
416 by considering the incident wave directions of $\beta = 0$, $\pi/2$ and π. Here, the optimal opening ratio
417 is selected, i.e. $\varepsilon = 3\%$. Due to the symmetry of the platform about the X-axis, only results for
418 OWC1 and OWC2 are plotted when the wave incidence angle is 0 and π for brevity, as shown
419 in Figs. 12(a) and (c), respectively. It can be seen in the low frequency domain ($kh \leq 1.76$), the
420 relative capturing widths of the front devices (i.e., OWC1 or OWC3 for $\beta = 0$; OWC2 for $\beta =$
421 π) are larger than that of the rear devices. The multi-scattered interactions among array devices
422 enhance the chamber hydrodynamics of the front devices. The relative capturing widths at $kh =$
423 1.13 increase greatly, especially for the incident wave direction $\beta = \pi/2$ and π. This is because
424 the incident wave period ($T = 2.1$ s) is close to the heave nature period of the platform ($T_{\text{heave}} =$
425 2.15 s) here, as shown in Table 9. The corresponding dynamic heave response of the platform
426 reaches the largest value, as shown in Fig. 9(c). In addition, the phase difference between the
427 chamber free surface elevation of the front devices ((i.e., OWC1 for $\beta = \pi/2$; OWC2 for $\beta = \pi$))
428 and the heave motion of the platform is larger than that of the rear device, i.e. the relative motion
429 is larger. While in the intermediate frequency domain ($1.76 \leq kh \leq 2.5$), the relative capturing
430 widths of the rear OWCs become larger. The maximum relative capturing widths of the rear
431 device occur at $kh = 2.0$ ($\beta = 0$) and $kh = 2.42$ ($\beta = \pi/2$ and π), respectively.

432 In order to further illustrate the capability of the OWCs, the total pneumatic power in the
433 prototype is shown in Fig. 13. It can be seen that the total pneumatic power increases with the
434 decrease of kh. And the total pneumatic power is over 200 kW in the frequency domain $kh \leq$
435 2.5.



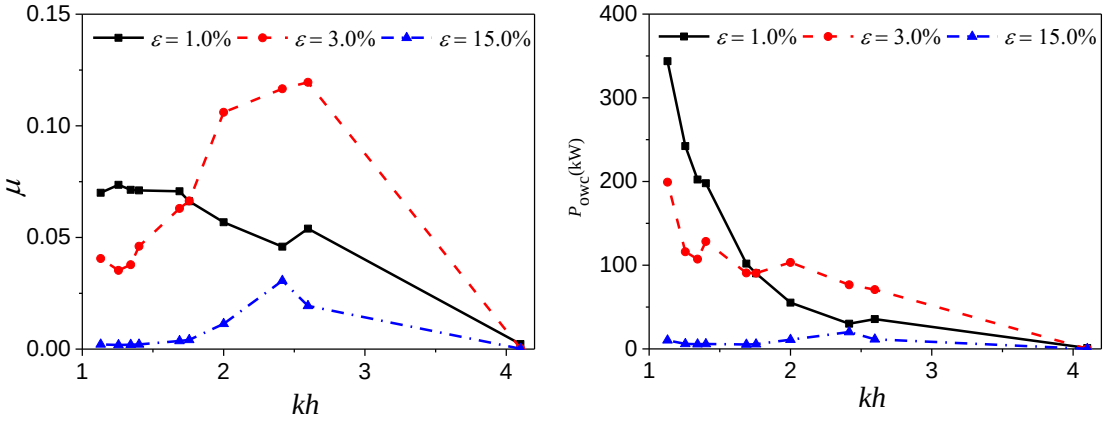
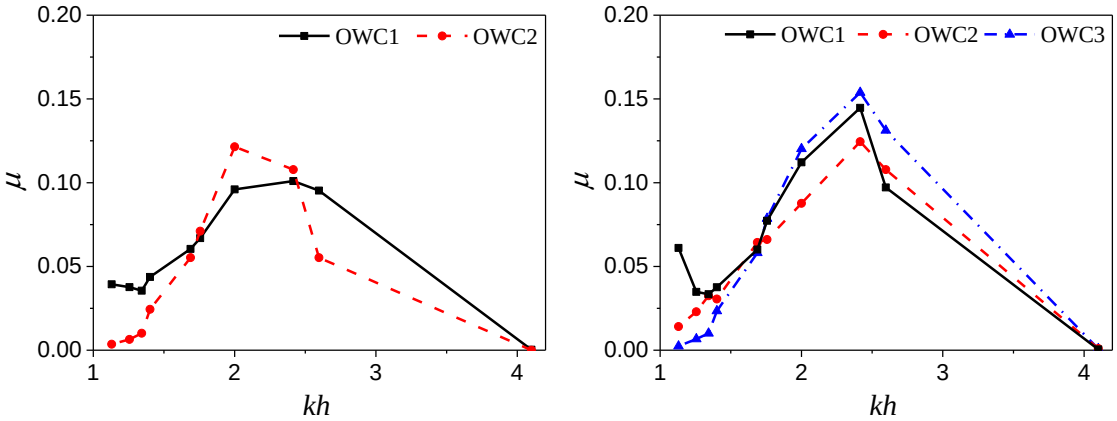
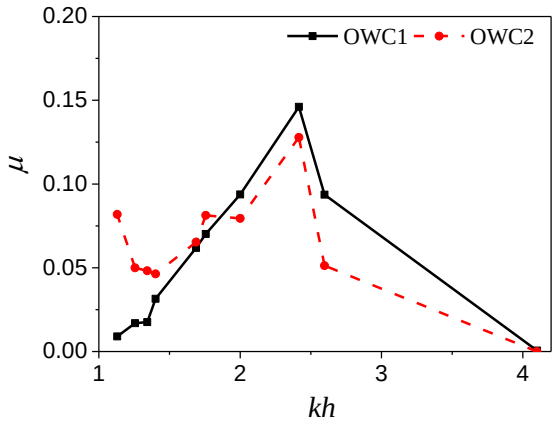


Fig. 11 Effect of the chamber opening ratio on the (a) chamber air pressure, (b) free surface elevation, (c) relative capturing width and (d) prototype pneumatic power (scale factor $50^{3.5}$) of the OWC1 ($\beta = 0$).





(c)

Fig. 12 Relative capturing width of the OWCs for (a) $\beta = 0$, (b) $\beta = \pi/2$ and (c) $\beta = \pi$ ($\varepsilon = 3\%$).

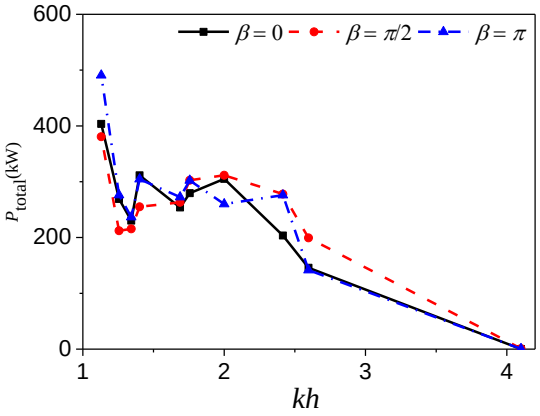


Fig. 13 Effects of the incident wave direction on the total pneumatic power in prototype ($\varepsilon = 3\%$, scale factor $50^{3.5}$).

4.3 Irregular wave tests

This section describes the effects of unidirectional irregular waves on the hydrodynamics of the FOWT-OWC platform. Both operational and survival sea states were tested, the parameters for which are shown in Table 8. The experimental time of each case was 30 minutes. The optimal opening ratio $\varepsilon = 3$ % was used. Other geometrical parameters of the experimental models are the same as in the previous section.

4.3.1 Time series of typical performance parameters

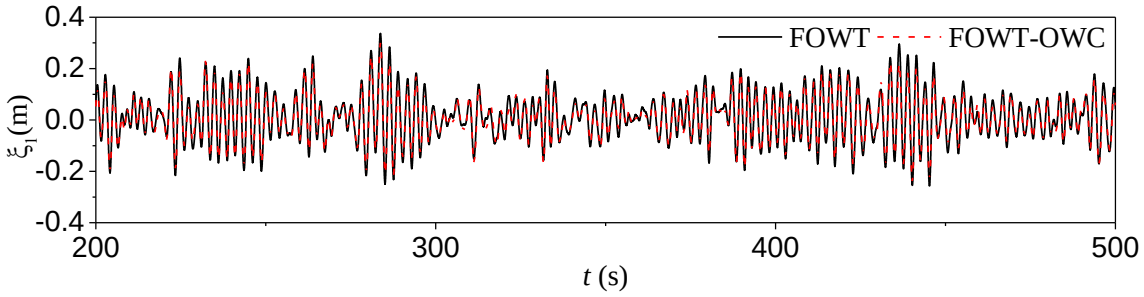
The time series of the key performance parameters for dynamic responses and wave energy capturing are discussed. The survival sea state $T_p = 2.54$s, $H_s = 0.21$ m was selected. Fig. 14

460 shows time histories of the surge, sway, heave, roll and pitch motions of the FOWT and FOWT-
461 OWC platforms. Only the time series in the 300s are illustrated. Comparing to surge and sway
462 motion, the heave, roll and pitch motions decrease more with the introduction of the OWC
463 devices.

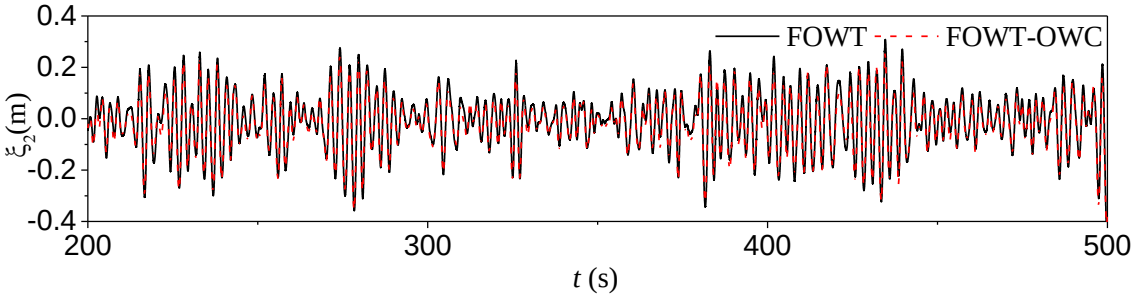
464 In order to further illustrate this phenomenon, Fig. 15 presents the recorded data in the
465 survival sea state. In each sub-plot, the non-dimensional motion amplitudes, based upon 30
466 minutes of irregular tests, are plotted against their probability of exceedance, Q_ξ. Here, $\triangle\xi_{1\text{-}5}/H$s– in which $\triangle\xi = (\xi_{creat} - \xi_{trough})/2$, is the averaged amplitude of each zero-crossing cycle.
468 It can be seen that the motion amplitudes of all degrees of freedom (DoF) motions decrease
469 with the introduction of the OWCs, especially for the extreme tail of the distribution. The
470 discrepancies in the heave, roll and pitch responses begin at a larger exceedance probability (Q_ξ
471 ≤ 0.2) when compared to the surge and sway motions ($Q_\xi \leq 0.8$). This is similar to the observed
472 results in regular wave conditions. This further confirms the stability improvement by applying
473 the proposed multi-functional integration.

474 Fig. 16 gives the time series of the chamber air pressure, the free surface elevation and the
475 pneumatic power of the OWC1 under the incident wave of $\beta = 0$. The pneumatic power is
476 calculated by Eq. (1). Comparing the results in Figs. 16(a) and (b), the chamber air pressure has
477 a phase lag of a quarter cycle to the free surface elevation inside the chamber. A similar
478 phenomenon was observed in an experimental simulation of a land-fixed OWC device [41]. In
479 Fig. 16(a), there exists negative air pressure inside the OWC chamber. This is associated with
480 the airflow drowning into the OWC chamber by the descending chamber free surface. The PTO
481 system obstructed this air entry, resulting in negative pressure inside the chamber. In Fig. 16(c),
482 the chamber air pressure reaches the maximum value $P_{air} = 432$ Pa at $t = 472.1$ s, where the
483 maximum pneumatic power also occurs, $P_{owc} = 2.67$ W. Under this test condition, the averaged
484 pneumatic power is 0.107 W. Thus, the relative capturing width of OWC1 is $\mu_{owc1}^{irr} = 1.87\%$. In
485 order to illustate the capability for capturing wave energy of the platform, Table 11 gives the
486 total relative capturing width ($\mu^{irr} = \mu_{owc1}^{irr} + \mu_{owc3}^{irr} + \mu_{owc3}^{irr}$) under three incident wave directions.
487 The platform under the incident wave of $\beta = \pi$ performs the highest total relative capturing

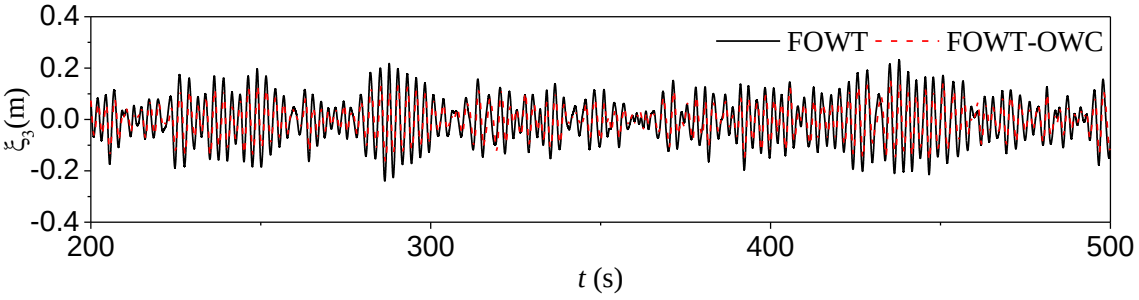
width. Fig.17 compares the total relative capturing width of the platform under regular and irregular waves. $T_{ir/irr}$ denotes the wave periods T or the peak wave periods T_p for the regular or irregular waves, respectively. It can be seen that the performance for wave energy capturing of the platform is better under regular waves. Yet, more irregular waves should be considered for a further analysis.



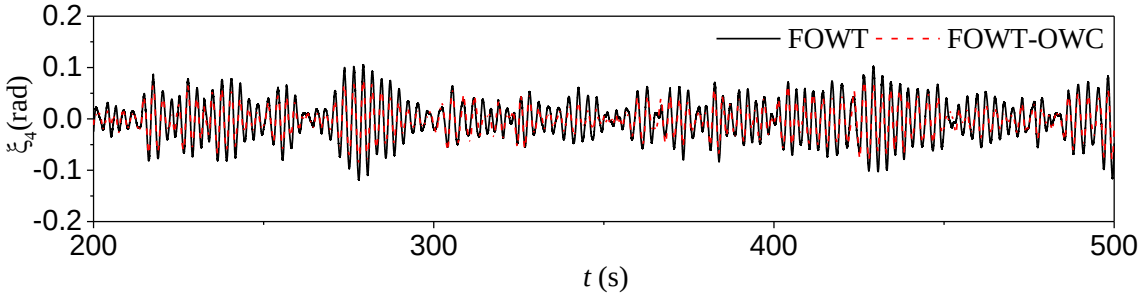
(a)



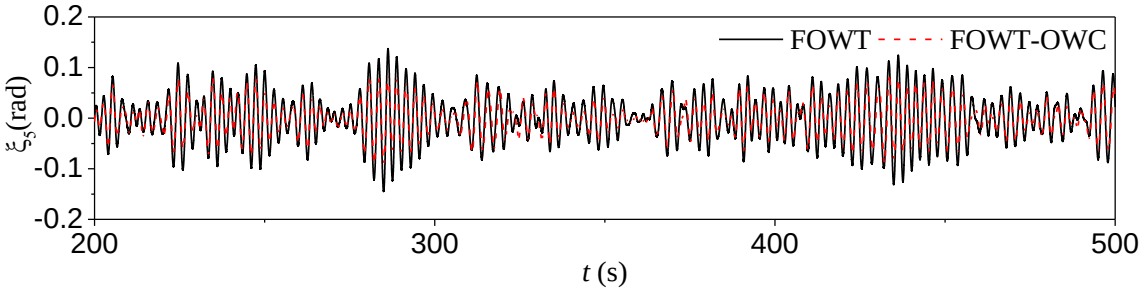
(b)



(c)

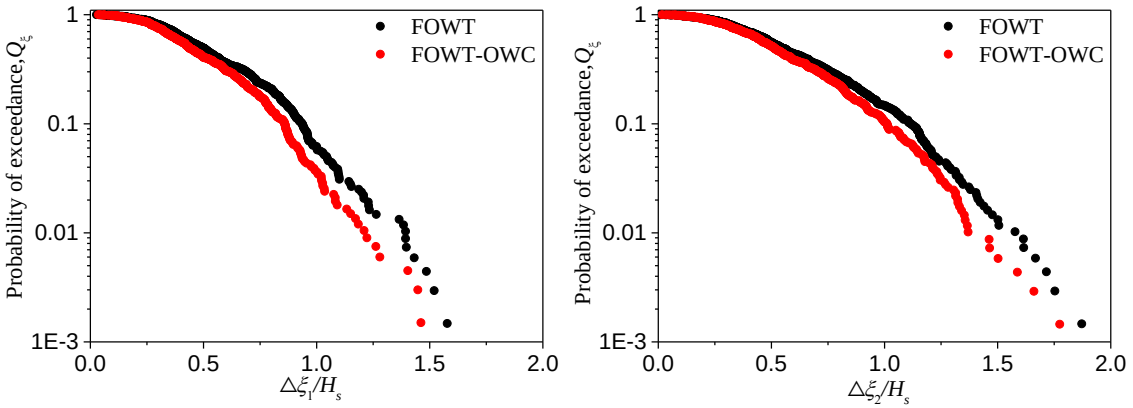


(d)

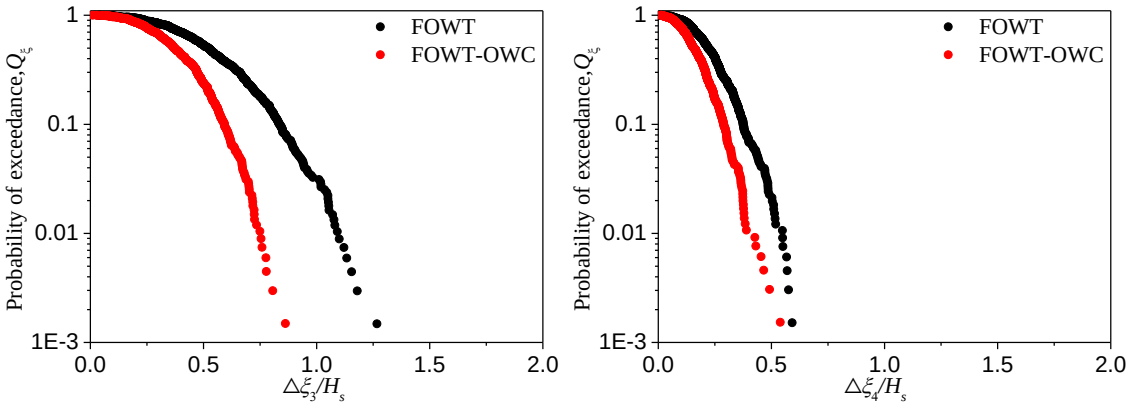


(e)

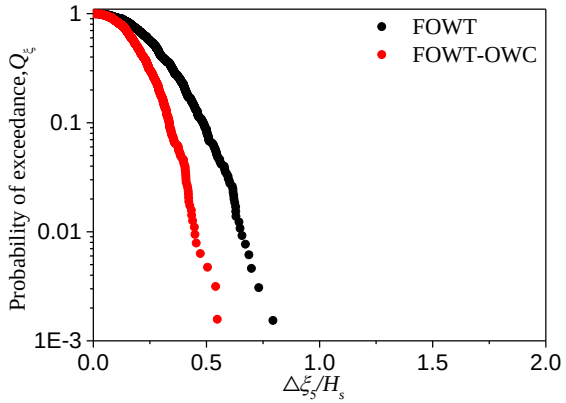
Fig.14 Time series of the (a) surge, (b) sway, (c) heave, (d) roll and (e) pitch motion of the FOWT and FOWT-OWC platforms (T_p = 2.54 s, H_s = 0.21 m).



(a) Surge (b) Sway

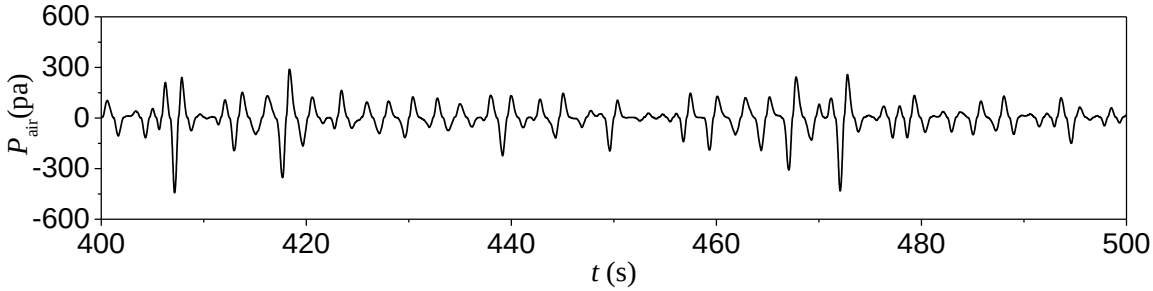


(c) Heave (d) Roll

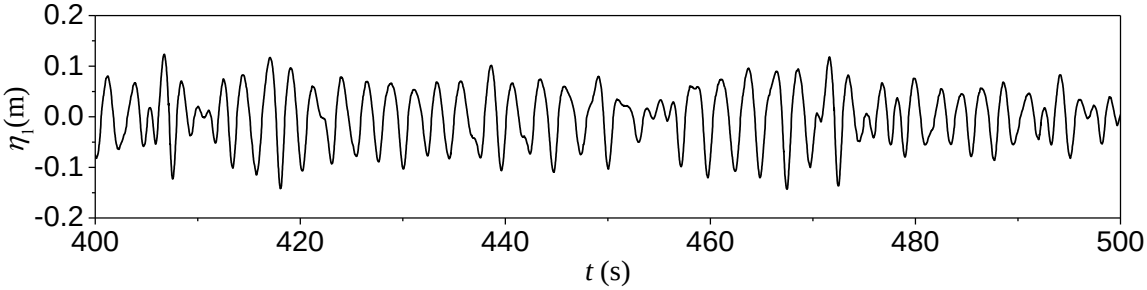


(e) Pitch

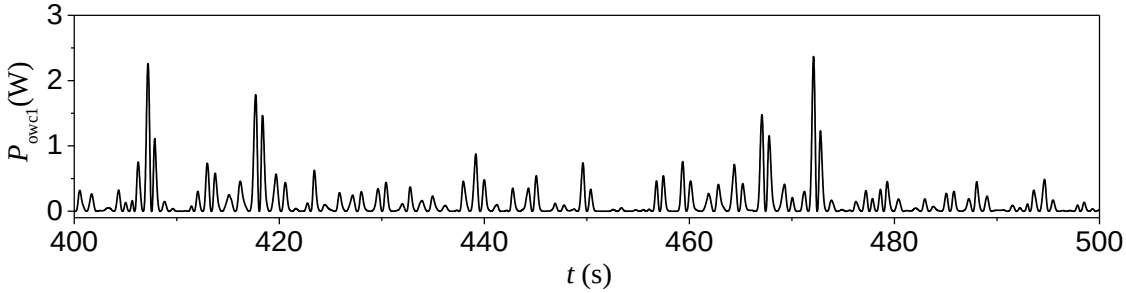
Fig.15 Motion response exceedance probabilities of the FOWT and FOWT-OWC platforms.



(a)



(b)



(c)

Fig.16 Time series of the (a) chamber air pressure, (b) chamber surface elevation and (c) pneumatic power

of OWC1 (T_p = 2.54 s, H_s = 0.21 m, β = 0).

Table 11. Total relative capturing width of the platform.

	T_p = 1.06 s, H_s = 0.03 m	T_p = 2.22 s, H_s = 0.178 m	T_p = 2.54 s, H_s = 0.21 m
$\beta = 0$	0.030	0.071	0.051
$\beta = \pi/2$	0.036	0.070	0.047
$\beta = \pi$	0.051	0.075	0.055

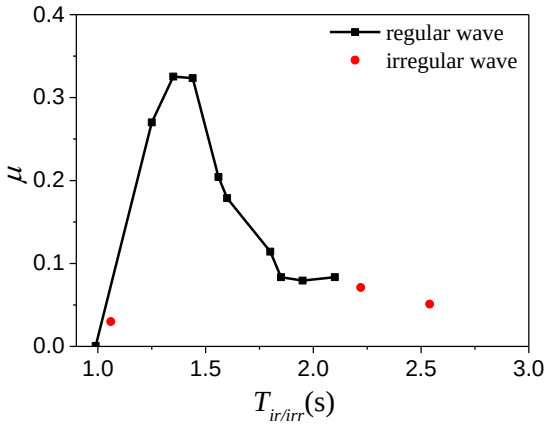


Fig.17 Total relative capturing width of the platform under regular and irregular waves (β = 0)

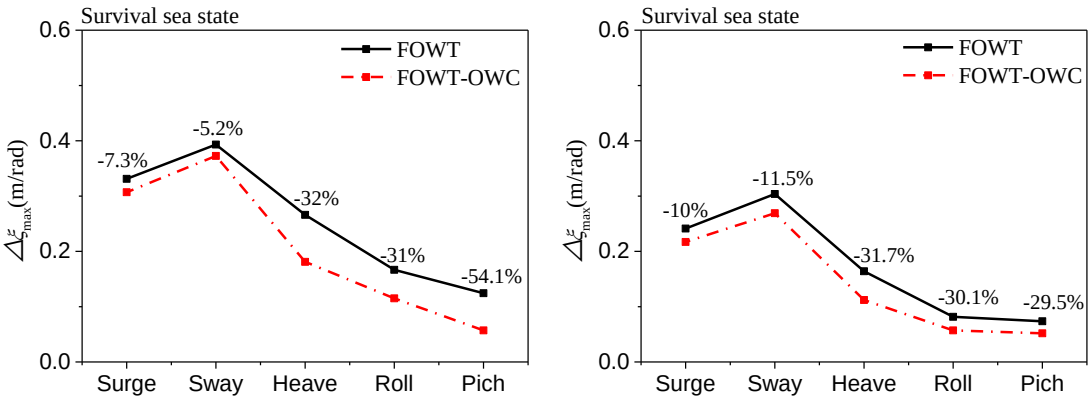
4.3.2 Hydrodynamic responses

Fig.18 shows the maximum response amplitudes of the FOWT and FOWT-OWC platforms under the survival and operational sea states. The response amplitude $\triangle\xi_{max}$ is the maximum amplitude across all zero-crossing periods. The corresponding variation ratios are also shown. The negative values represent the decrease in the motions, and the positive values mean the increase. It can be seen that the five DoF motions of the FOWT-OWC platform are all reduced under the survival sea state, with a reduction ratio larger than 29.5% in heave, roll and pitch motions. As discussed above, this results from the increase of the added mass and damping of the platform induced by the OWCs.

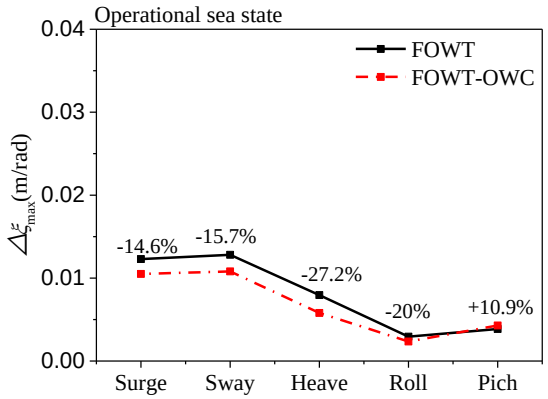
In addition, the maximum motion amplitude is found to be relatively small under the operational sea state; the magnitude is less than 0.015 as shown in Fig. 18(c) when compared

to 0.4 in Figs. 18 (a-b). It is found that the motions in surge, sway, heave and roll decreased by 14.6%, 15.7%, 27.2% and 20%, respectively. In contrast, the maximum pitch amplitudes are increased by 10.9%. The peak period T_p = 1.06 s in the operational sea state is close to that of the surrounding wave condition (kh = 2.6), leading to the large resonant pitch motion, as shown in Fig 9(e). Generally, the introductions of the OWCs can enhance the stability of the platform, especially under the survival sea states.

Fig. 19 shows the maximum nacelle and deck accelerations of the FOWT and FOWT-OWC platforms under the survival and operational sea states. The parameter $H_p^2T_p$ is used to approximate the incident wave energy along the X-axis. It is clear that the acceleration of the nacelle is larger than that of the deck. This is reasonable given that the nacelle has a larger rotational radius. Compared to the results of the FOWT, both nacelle and deck accelerations decrease with the introduction of the OWCs, especially in the survival sea states. As discussed above, the decreases in the motion amplitudes would lead to a smaller value of both the velocity and acceleration of the platform. It is well-established that the nacelle accelerations and tilts are governed by the performance of the wind turbine. Thus, both the nacelle accelerations and tilts of the FOWT-OWC are discussed shown in Fig. 20. It can be seen that the incident wave direction $\beta = \pi$ is the less favorable situation for the wind turbine operation.



(a) T_p = 2.54 s, H_s = 0.21 m (b) T_p = 2.22 s, H_s = 0.178 m



(c) T_p = 1.06 s, H_s = 0.03 m

Fig.18 Maximum response amplitudes of the FOWT and FOWT-OWC platforms under survival and operational sea states.

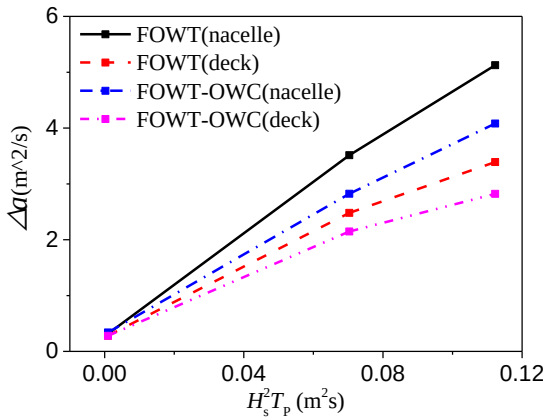
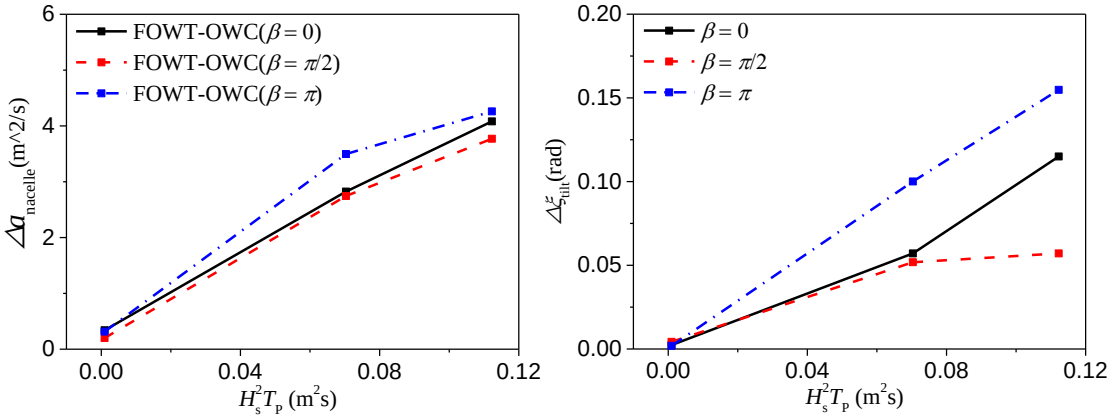


Fig.19 Maximum nacelle and deck accelerations of the FOWT and FOWT-OWC platforms under survival and operational sea states ($\beta = 0$).



(a) (b)

Fig.20 Effects of the incident wave direction on maximum nacelle (a) acceleration and (b) tilt of the FOWT-OWC platforms under survival and operational sea states.

5. Conclusions

The multi-functional offshore platform is a promising concept for not only reducing construction costs but also improving overall performance. This paper proposed a semi-submersible wind turbine foundation integrated with three OWCs. The hydrodynamic performance in terms of the reduced platform motion and the wave energy capturing are assessed. A carefully instrumented experiment was carried out in a wave flume at a scale of 1:50. The hydrodynamic investigations on platform responses and wave energy capturing were performed under a series of regular and irregular conditions. The effects of the chamber opening ratio and the incident wave direction were studied systematically. The following conclusions from the experiments are summarized

1. From the RAO analysis, the introduction of the OWCs can not only capture wave energy but also reduce the heave, roll and pitch motions, especially for long waves $kh \leq 2.0$, $kh \leq 1.4$ and $kh \leq 1.76$, respectively. A phenomenon for the anti-phase oscillation of the chamber water columns is observed, which leads to a larger pitch amplitude of the FOWT-OWC platform.
2. The chamber opening ratio is optimized to be at $\varepsilon = 3\%$, which produces the maximum relative capturing width in the intermedia and high frequency domains. In the low frequency domain, regardless of the direction of the incident wave, the relative capturing width of the front OWC is always larger than that of the rear one.
3. From the survival sea state tests, the maximum response amplitudes of all five DoF motions decrease when compared to the FOWT platform, especially for the heave, roll and pitch. The nacelle accelerations and tilts observed suggest that the incident wave with direction $\beta = \pi$ could perform the worst damage to the wind turbine.

The present study has shown the hydrodynamics of a horizontal-moored FOWT-OWC platform. The effect of wind is not considered. Therefore, a more extensive coupling analysis will be performed by considering the combined interactions of wave, wind and current in the

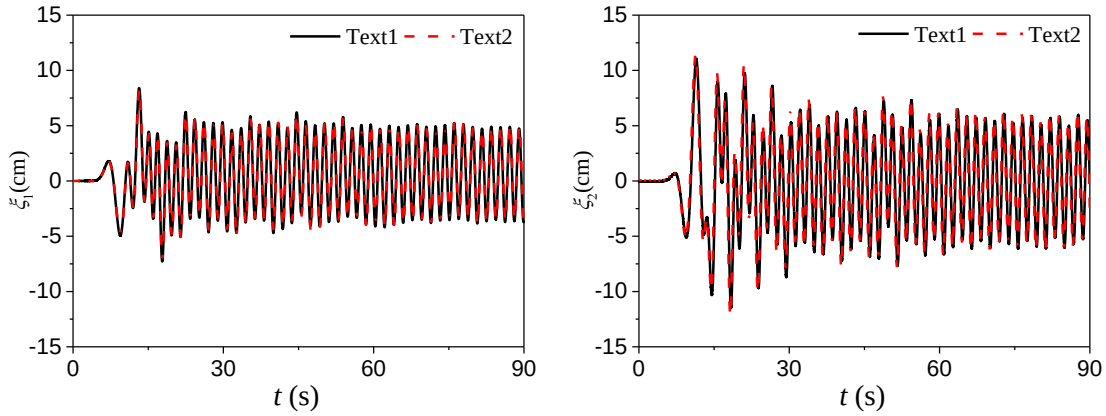
future.

Acknowledgments

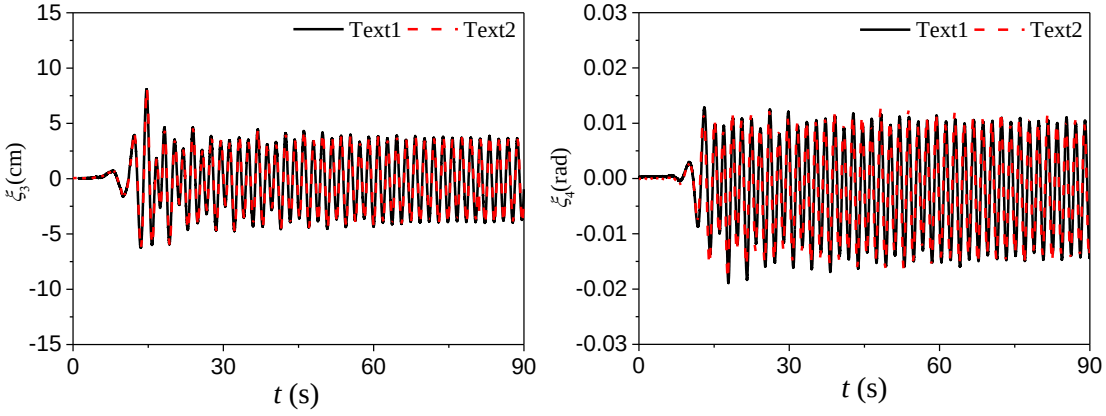
This work is supported by the National Natural Science Foundation of China (Nos. U22A20242 and 52271260) and Liaoning Revitalization Talents Program (Grant No. XLYC2002033).

Appendix A. Experimental repeatability

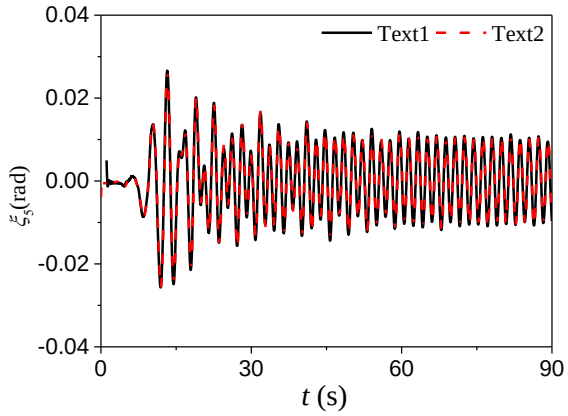
The time histories of the measured results of the FOWT and FOWT-OWC platforms in Figs. A1 and A5. Figs. A1 and A3 show the time series of the surge, sway, heave, roll and pitch motions of the platform. Figs. A2 and A5 illustrate the time series of the desk and nacelle accelerations in the X- and Z-axis. Fig. A4 gives the time histories of the chamber air pressure P_{air1} and free surface elevation η_1 of OWC1 for the incident wave direction $\beta = 0$ and $\pi/2$.



(a) (b)

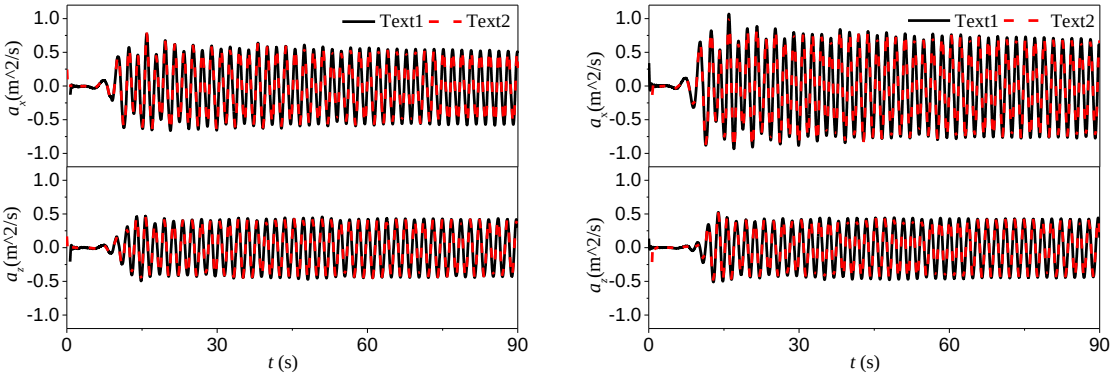


(c) (d)



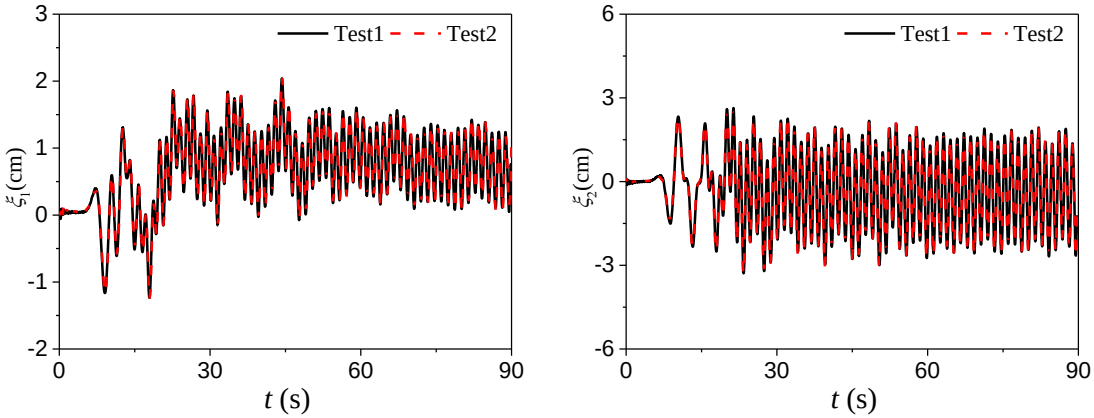
(e)

Fig. A1 Time series of the (a) surge, (b) sway, (c) heave, (d) roll and (e) pitch motions of the FOWT platform at kh = 1.34.

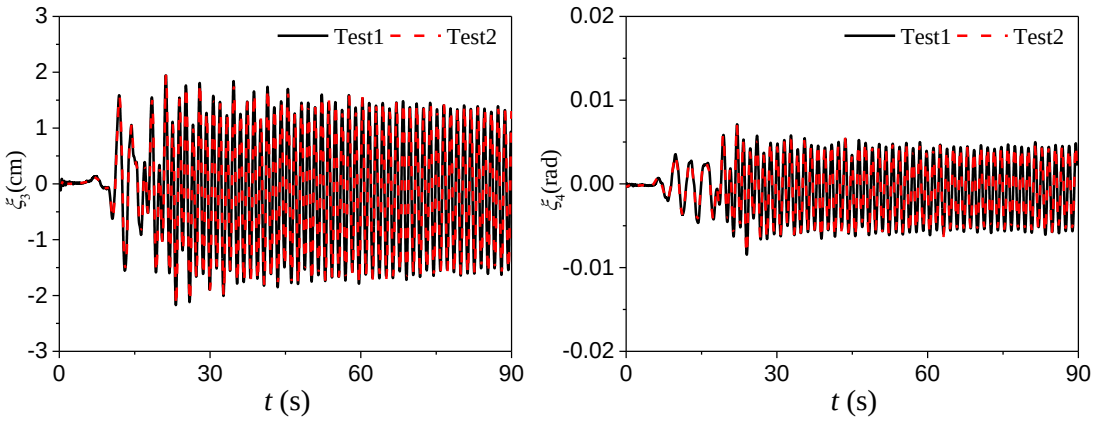


(a) deck (b) nacelle

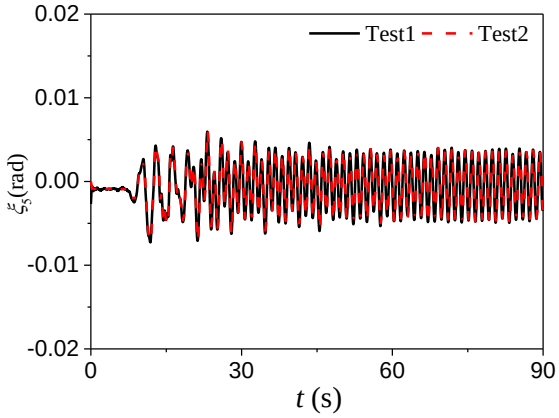
Fig. A2 Time series of the X- and Z-axis accelerations on (a) desk and (b) nacelle at kh = 1.34 (β = 0).



(a) (b)

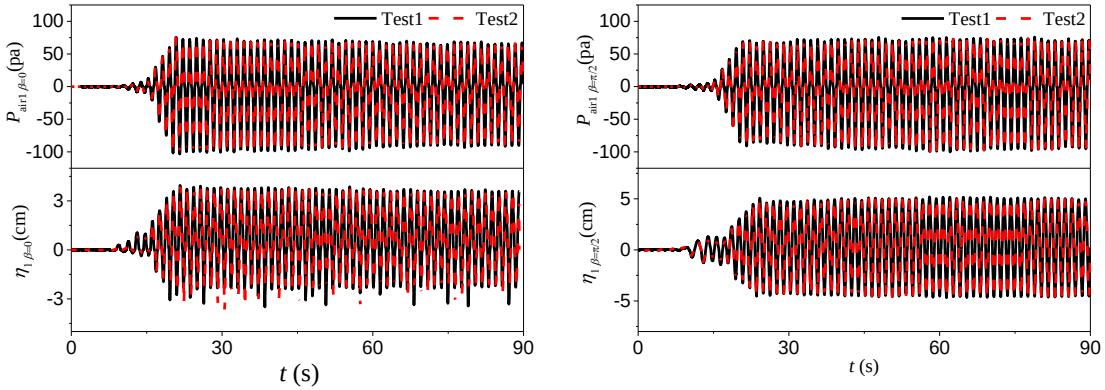


(c) (d)



(e)

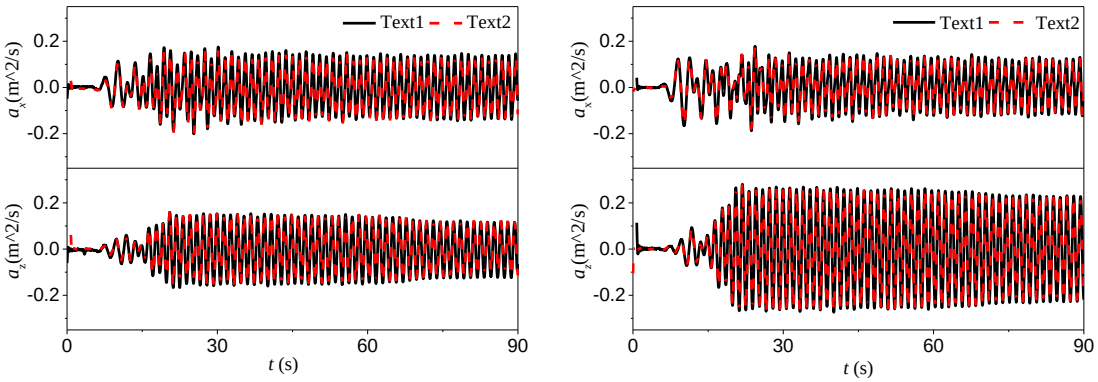
Fig. A3 Time series of the (a) surge, (b) sway, (c) heave, (d) roll and (e) pitch motions of the FOWT-OWC platform at kh = 2.42 (ε = 3 %).



(a) (b)

Fig. A4 Time series of the chamber air pressure and free surface elevation of the OWC1 for the incident

wave direction (a) $\beta = 0$ and (b) $\beta = \pi/2$ at $kh = 2.42$ ($\varepsilon = 3$ %)



(a) deck (b) nacelle

Fig. A5 Time series of the X- and Z-axis accelerations on the (a) desk and (b) nacelle at $kh = 2.42$ ($\beta = 0$).

References

[1] Camera FL. Global weighted average total installed costs, capacity factors and LCOE 2010-2020. International Renewable Energy Agency; 2021.

[2] Sijtsma J. Stability assessment of a floating hybrid wind-wave platform: a frequency signal analysis 2020.

[3] Ahamed R, McKee K, Howard I. Advancements of wave energy converters based on power take off (PTO) systems: A review. Ocean Eng. 2020;204:107248.

[4] Zhao X, Zhang Y, Li M, Johanning L. Hydrodynamic performance of a Comb-Type Breakwater-WEC system: An analytical study. Renew Energy. 2020;159:33.

[5] Li Y, Liu S, Xu C, Li D, Shi H. Experimental study on the cylindrical oscillating water column device. Ocean Eng. 2022;246:110523.

[6] Kalogeri C, Galanis G, Spyrou C, Diamantis D, Baladima F, Koukoula M, et al. Assessing the European offshore wind and wave energy resource for combined exploitation. Renew Energy. 2017;101:244-64.

[7] Azzellino A, Lanfredi C, Riefolo L, De Santis V, Contestabile P, Vicinanza D. Combined exploitation of offshore wind and wave energy in the Italian seas: a spatial planning approach. Frontiers in Energy Research. 2019;7:42.

[8] Lund H. Large-scale integration of optimal combinations of PV, wind and wave power into the electricity supply. Renew Energy. 2006;31:503-15.

[9] Kumawat A, Karmakar D, Guedes Soares C. Numerical investigation of semi-submersible floating wind turbine combined with flap-type wecs. Proceedings of the Fourth International Conference in Ocean Engineering (ICOE2018): Springer; 2019. p. 793-805.

[10] Pérez-Collazo C, Greaves D, Iglesias G. A review of combined wave and offshore wind energy. Renewable Sustainable Energy Reviews. 2015;42:141-53.

[11] Hu J, Zhou B, Vogel C, Liu P, Willden R, Sun K, et al. Optimal design and performance analysis of a hybrid system combing a floating wind platform and wave energy converters. Appl

Energy. 2020;269:114998.
[12] Zhou B, Hu J, Jin P, Sun K, Li Y, Ning D. Power performance and motion response of a floating wind platform and multiple heaving wave energy converters hybrid system. Energy. 2022;265:126314.
[13] He Z, Ning D, Gou Y, Zhou Z. Wave energy converter optimization based on differential evolution algorithm. Energy. 2022;246:123433.
[14] Zhou Y, Ning D, Liang D, Cai S. Nonlinear hydrodynamic analysis of an offshore oscillating water column wave energy converter. Renew Sust Energ Rev. 2021b;145:111086.
[15] Falnes J, Kurniawan A. Ocean waves and oscillating systems: linear interactions including wave-energy extraction: Cambridge University Press; 2020.
[16] Wan L, Gao Z, Moan T. Experimental and numerical study of hydrodynamic responses of a combined wind and wave energy converter concept in survival modes. Coast Eng. 2015;104:151-69.
[17] Si Y, Chen Z, Zeng W, Sun J, Zhang D, Ma X, et al. The influence of power-take-off control on the dynamic response and power output of combined semi-submersible floating wind turbine and point-absorber wave energy converters. Ocean Eng. 2021;227:108835.
[18] Gao Z, Moan T, Wan L, Michailides C. Comparative numerical and experimental study of two combined wind and wave energy concepts. Journal of Ocean Engineering and Science. 2016;1:36-51.
[19] Kushwah S. An oscillating water column (OWC): the wave energy converter. Journal of The Institution of Engineers (India): Series C. 2021;102:1311-7.
[20] Zhou Y, Ning D, Chen L, Mayon R, Zhang C. Experimental investigation on an OWC wave energy converter integrated into a floating offshore wind turbine. Energy Conversion and Management. 2023;276:116546.
[21] Konispoliatis D, Mazarakos T, Mavrakos S. Hydrodynamic analysis of three–unit arrays of floating annular oscillating–water–column wave energy converters. Appl Ocean Res. 2016;61:42-64.
[22] Konispoliatis DN, Katsaounis GM, Manolas DI, Soukissian TH, Polyzos S, Mazarakos TP, et al. REFOS: A Renewable Energy Multi-Purpose Floating Offshore System. Energies. 2021;14:3126.
[23] M'zoughi F, Aboutalebi P, Garrido I, Garrido AJ, De La Sen M. Complementary Airflow Control of Oscillating Water Columns for Floating Offshore Wind Turbine Stabilization. Mathematics. 2021;9:1364.
[24] Li L, Ruzzo C, Collu M, Yan G, Arena F. Analysis of the Coupled Dynamic Response of an Offshore Floating Multi-Purpose Platform for the Blue Economy. Ocean Eng. 2020;217:107943.
[25] Zhao X, Xue R, Geng J, Göteman M. Analytical investigation on the hydrodynamic performance of a multi-pontoon breakwater-WEC system. Ocean Eng. 2021;220:108394.
[26] Ning DZ, Wang RQ, Zhang CW. Numerical Simulation of a Dual-Chamber Oscillating Water Column Wave Energy Converter. Sustainability. 2017;9:1599.
[27] Han M, Wang C. Coupled analytical-numerical approach for determining hydrodynamic responses of breakwater with multiple OWCs. Marine Structures. 2021;80:103097.

[28] Zhu H, Hu C, Sueyoshi M, Yoshida S. Integration of a semisubmersible floating wind turbine and wave energy converters: an experimental study on motion reduction. Journal of Marine Science and Technology. 2019;25.
[29] Zhang D, Chen Z, Liu X, Sun J, Yu H, Zeng W, et al. A coupled numerical framework for hybrid floating offshore wind turbine and oscillating water column wave energy converters. Energy Conversion and Management. 2022;267:115933.
[30] Sarmiento J, Iturrioz A, Ayllón V, Guanche R, Losada IJ. Experimental modelling of a multi-use floating platform for wave and wind energy harvesting. Ocean Eng. 2019;173:761-73.
[31] Fenu B, Bonfanti M, Bardazzi A, Pilloton C, Lucarelli A, Mattiazzo G. Experimental investigation of a Multi-OWC wind turbine floating platform. Ocean Eng. 2023;281:114619.
[32] Aubault A, Alves M, Sarmento An, Roddier D, Peiffer A. Modeling of an oscillating water column on the floating foundation WindFloat. In: International Conference on Offshore Mechanics and Arctic Engineering. Rotterdam2011. p. 235-46.
[33] Soares CG. Offshore structure modelling. World Scientific1995.
[34] Ning DZ, Wang RQ, Chen LF, Sun K. Experimental investigation of a land-based dual-chamber OWC wave energy converter. Renew Sust Energ Rev. 2019;105:48-60.
[35] Falcão AF, Henriques JC. The spring-like air compressibility effect in oscillating-water-column wave energy converters: Review and analyses. Renew Sust Energ Rev. 2019;112:483-98.
[36] Yu T, Guo Q, Shi H, Li T, Meng X, He S, et al. Experimental investigation of a novel OWC wave energy converter. Ocean Eng. 2022;257:111567.
[37] Shangguan L, Lu K, Wang H. Research on Laboratory Test Method of Wave Energy Converter Wave-Wire Conversion Ratio in Irregular Waves. Energies. 2023;16:1001.
[38] Paz M. Structural dynamics: theory and computation: Springer Science & Business Media; 2012.
[39] Elhanafi A, Macfarlane G, Fleming A, Leong Z. Experimental and numerical measurements of wave forces on a 3D offshore stationary OWC wave energy converter. Ocean Eng. 2017;144:98-117.
[40] Elhanafi A, Chan JK. Experimental and numerical investigation on wave height and power take–off damping effects on the hydrodynamic performance of an offshore–stationary OWC wave energy converter. Renew Energy. 2018;125:S0960148118302830.
[41] Liu Z, Xu C, Shi H, Qu N. Wave-flume tests of a model-scaled OWC chamber-turbine system under irregular wave conditions. Appl Ocean Res. 2020;99:102141.